# Multichannel Mueller Matrix Ellipsometry for Simultaneous Real-Time Measurement of Bulk Isotropic and Surface Anisotropic Complex Dielectric Functions of Semiconductors

Chi Chen, Ilsin An, and R.W. Collins

*Department of Physics and Materials Research Institute, The Pennsylvania State University, University Park, Pennsylvania 16802, USA*

(Received 13 February 2003; published 28 May 2003)

We have applied a dual rotating-compensator multichannel ellipsometer to acquire spectra ($\sim$ 2.0–4.6 eV) in all 16 elements of the Mueller matrix associated with a specularly reflecting surface, in a minimum time of 0.25 s. In this initial study, such results have been collected for the (110) silicon surface at an incidence angle of $\sim$70° and have been used to derive spectra in the bulk isotropic dielectric function $\varepsilon_b = \varepsilon_{1b} - i\varepsilon_{2b}$ and the surface-induced dielectric function anisotropy $\Delta\varepsilon = \Delta\varepsilon_1 - i\Delta\varepsilon_2$. Thus, this instrument shows promise for simultaneous real-time measurement of $\varepsilon_b$ and $\Delta\varepsilon$ spectra in oblique reflection during the fabrication of semiconductor structures having bulk isotropic components.

DOI: 10.1103/PhysRevLett.90.217402 PACS numbers: 78.20.Ci, 07.60.Fs, 42.25.Ja, 78.68.+m

The dielectric functions of semiconductors provide insights into bulk optical processes, as well as useful information on bulk material characteristics such as composition, doping, grain size, ordering, and temperature [1]. As a result, real-time spectroscopic ellipsometry (SE) at oblique incidence ($\theta_a \sim 60°$–$80°$ from the surface normal) has been developed as a powerful probe of optically isotropic semiconductors during their fabrication and processing [2]; however, such capabilities have yet to be fully developed for bulk anisotropic semiconductors. Similarly, the surface-induced anisotropy spectra for single-crystal semiconductors that are isotropic in the bulk provide insights into surface optical processes, as well as useful information on surface termination [3]. As a result, real-time reflectance difference (RD), usually performed at one wavelength and normal incidence ($\theta_a \sim 0°$), has been developed to probe such surfaces [4]. Real-time SE and RD are complementary and in general require separate optical access and probe beams. In a notable exception, Ebert *et al.* have performed simultaneous real-time SE and RD spectroscopy (RDS) by rotating the incident beam polarizer synchronously with the sample [5].

We have developed a dual rotating-compensator multichannel ellipsometer that provides spectra from 2.0 to 4.6 eV in all 16 elements of the $4 \times 4$ Mueller matrix for a fixed-position reflecting sample in a time of 0.25 s [6,7]. From the Mueller matrix, the Jones matrix of the sample and the depolarization characteristics of the reflected beam can be extracted using multiple, independent expressions. For single-crystal semiconductors that are isotropic in the bulk, the bulk dielectric function $\varepsilon_b = \varepsilon_{1b} - i\varepsilon_{2b}$ can be deduced from the Jones matrix along with the surface dielectric function difference $\Delta\varepsilon = \Delta\varepsilon_1 - i\Delta\varepsilon_2$ for optical fields vibrating along orthogonal principal axes in the plane of the anisotropic surface. Advantages over earlier approaches include the use of a single beam and fixed sample, and the full spectroscopic capability. In addition, for semiconductors that are anisotropic in the bulk, the principal components of the dielectric tensor can be deduced from the Jones matrix within geometric restrictions [8]. Thus, a real-time SE capability is now available for these materials.

Figure 1 depicts the design of the multichannel ellipsometer, based on the dual rotating-compensator principle [7]. In this design, $MgF_2$ biplate compensators on the incident and reflection sides of the instrument are rotated synchronously at $5\omega_B$ and $3\omega_B$, respectively, where the fundamental mechanical rotation frequency is $\omega_B/2\pi = 2$ Hz. Data acquisition involves reading the linear photodiode array detector 36 times per optical cycle, given by $\pi/\omega_B = 0.25$ s. From these 36 readouts, spectra in the dc Fourier coefficient ($I_0$) and the first (17 cosine, 18 sine) $2n\omega_B$ Fourier coefficients ($\alpha_{2n}$, $\beta_{2n}$) (normalized by the dc coefficient by convention) for the irradiance waveform can be determined. Then the Mueller matrix elements can be established from the 25 nonzero coefficients $\{I_0, (\alpha_{2n}, \beta_{2n}); n = 1, \ldots, 8, 10, 11, 13, 16\}$ [6].

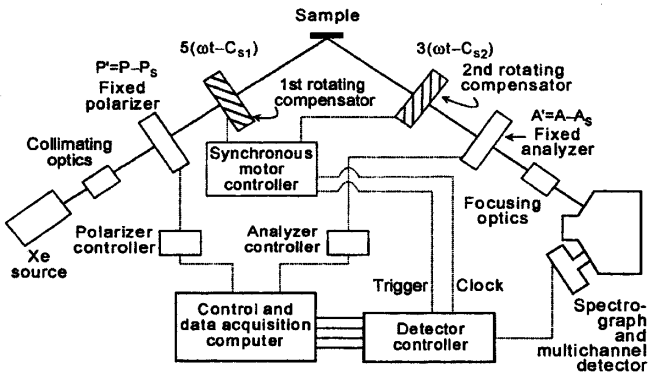


FIG. 1. Schematic diagram of the dual rotating-compensator multichannel ellipsometer.

  

In this study, the bulk isotropic and surface anisotropic optical properties of a reflecting semiconductor are derived from the ratios of complex amplitude reflection coefficients $\rho_{pp} \equiv r_{pp}/r_{ss} = \tan\psi_{pp}\exp(i\Delta_{pp})$, $\rho_{ps} \equiv r_{ps}/r_{ss} = \tan\psi_{ps}\exp(i\Delta_{ps})$, and $\rho_{sp} \equiv r_{sp}/r_{ss} = \tan\psi_{sp}\exp(i\Delta_{sp})$ that define the (2,2)-normalized complex Jones matrix. Because six real quantities define this Jones matrix, whereas 15 real elements $m_{ij}$ define the (1,1)-normalized $4 \times 4$ Mueller matrix $\mathbf{m}$, the former can be deduced by multiple expressions. The following are the most useful for weakly anisotropic semiconductors:

$$\rho_{pp} = [(m_{33} + m_{44}) + i(m_{34} - m_{43})]/D_1, \tag{1a}$$

$$|\rho_{pp}|^2 = D_2/D_1, \tag{1b}$$

$$\rho_{sp} = [(m_{13} - m_{23}) + i(m_{14} - m_{24})]/D_1 \tag{2a}$$

$$= \{(m_{33} + m_{44})[(m_{31} + m_{32}) + i(m_{41} + m_{42})] - (m_{34} - m_{43})[(m_{41} + m_{42}) - i(m_{31} + m_{32})]\}/D_1D_2, \tag{2b}$$

$$\rho_{ps} = [(m_{31} - m_{32}) - i(m_{41} - m_{42})]/D_1 \tag{3a}$$

$$= \{(m_{33} + m_{44})[(m_{13} + m_{23}) - i(m_{14} + m_{24})] + (m_{34} - m_{43})[(m_{14} + m_{24}) + i(m_{13} + m_{23})]\}/D_1D_2, \tag{3b}$$

where

$$D_1 = p - m_{12} - m_{21} + m_{22}, \tag{4a}$$

$$D_2 = p + m_{12} + m_{21} + m_{22}. \tag{4b}$$

The degree of polarization $p$ is incorporated based on the assumption of a random depolarization process and is determined from all elements of $\mathbf{m}$:

$$p = (b^2 + c)^{1/2} - b, \tag{5a}$$

$$b = (m_{22} - m_{12} - m_{21})/3, \tag{5b}$$

$$c = [(m_{22} - m_{12} - m_{21})^2 + (m_{13} - m_{23})^2 + (m_{14} - m_{24})^2 + (m_{31} - m_{32})^2 + (m_{41} - m_{42})^2 + (m_{34} - m_{43})^2 + (m_{33} + m_{44})^2]/3. \tag{5c}$$

As an example, Fig. 2 shows experimental spectra in $\rho_{pp}$, $\rho_{ps}$, $\rho_{sp}$, and $p$, as deduced from the Mueller matrix for (110) Si, which was chosen as a first test case because its surface anisotropy has been well studied by RDS [3]. These spectra were collected at 25 °C with an angle of incidence of $\theta_a = 69.90° \pm 0.05°$, and the angle $\phi$ between the surface [001] principal axis and the $p$-polarization direction was set at 45° to maximize the amplitudes of $\rho_{ps}$ and $\rho_{sp}$ [see Eq. (6)]. The sample was mounted in a windowless cell and etched using 5 vol% HF in $CH_3OH$ just before the measurement, which was then performed under a flow of $N_2$. The spectra in the Mueller matrix for the data set of Fig. 2 were collected in 12 s, taking an average of 48 detector waveforms over 24 mechanical cycles. In Fig. 2, $\rho_{pp}$ was obtained from Eq. (1a), whereas the low energy ($< 3$ eV) parts of $\mathrm{Re}(\rho_{sp})$ and $\mathrm{Re}(\rho_{ps})$ were obtained from Eqs. (2b) and (3a), respectively. For $\mathrm{Re}(\rho_{sp})$ and $\mathrm{Re}(\rho_{ps})$ at higher energy and for $\mathrm{Im}(\rho_{sp})$ and $\mathrm{Im}(\rho_{ps})$ over the full energy range, the results from Eqs. (2a) and (3a) were averaged with those from Eqs. (2b) and (3b), respectively. This overall approach provided the highest accuracy spectra in $\rho_{sp}$ and $\rho_{ps}$. The deviations of $p$ from unity in Fig. 2 are attributed to polarization mixing errors, e.g., finite energy resolution, angle of incidence spread, and spectrograph stray light.

Figure 3 shows the real and imaginary parts of the bulk dielectric function $\varepsilon_b$ and the surface anisotropic response $(\Delta\varepsilon)d \equiv (\varepsilon_{1\bar{1}0} - \varepsilon_{001})d$ for (110) Si, derived from the results of Fig. 2. The spectra in $\varepsilon_b$ are determined assuming a single abrupt interface between the ambient and the bulk Si, neglecting surface overlayers and anisotropy. The spectra in $(\Delta\varepsilon)d$ can be modeled assuming an ultrathin uniaxial layer (of thickness $d \sim 4$ Å) with its optic axis lying in the plane of the crystal. From this model, one can derive

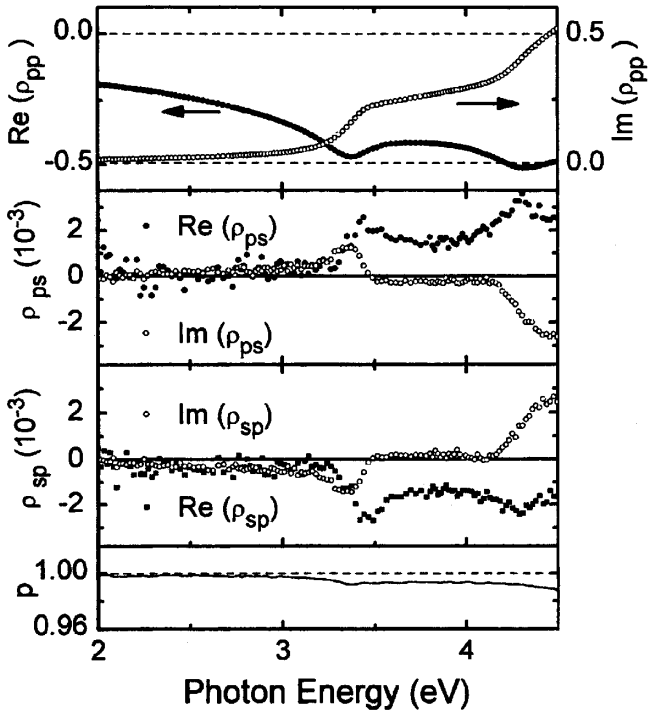


FIG. 2. Real and imaginary parts of the complex amplitude reflection ratios, $\rho_{pp}$, $\rho_{ps}$, and $\rho_{sp}$ (top to bottom), and the degree of polarization $p$ measured for a clean (110) Si surface at an angle of incidence of $\theta_a = 69.90° \pm 0.05°$. All spectra were derived from Fourier coefficients collected in 12 s.

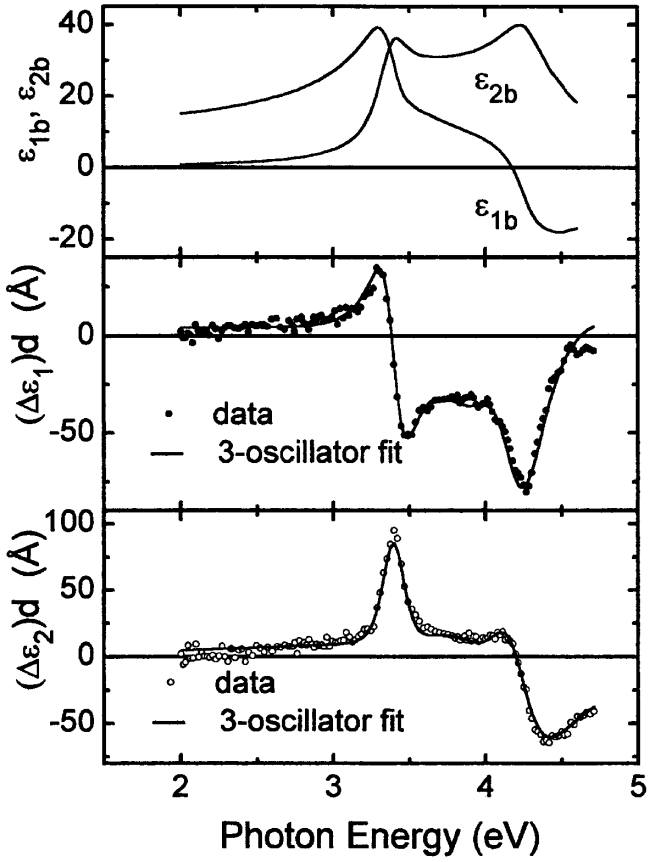


FIG. 3. Real and imaginary parts of the complex dielectric function $\varepsilon_b$, and the complex surface anisotropic optical response $(\Delta\varepsilon)d$ for a clean (110) Si surface derived from the spectra of Fig. 2. The solid lines in the lower panels represent a fit using three oscillators.

$$\rho_{ps} = -\rho_{sp} = \frac{4\pi i(d/\lambda)\Delta\varepsilon \sin\phi \cos\phi \cos\theta_a \cos\theta_b}{(\varepsilon_b^{1/2}\cos\theta_a + \cos\theta_b)(\varepsilon_b^{1/2}\cos\theta_b - \cos\theta_a)}, \tag{6}$$

to first order in $(d/\lambda)$, where $\lambda$ is the wavelength [9]. In Eq. (6), $\theta_b$ is the complex angle of transmission into the bulk Si substrate. Figure 2 provides support for this model to the extent that the measured $\rho_{ps}$ and $\rho_{sp}$ are closely opposite in sign. In fact, to obtain $(\Delta\varepsilon)d$ in Fig. 3 with the highest possible accuracy and precision, we assume that $\rho_{ps} = -\rho_{sp}$ and average all four results for each of $\mathrm{Re}(\rho_{ps})$ and $\mathrm{Im}(\rho_{ps})$ using Eqs. (2) and (3).

Figure 4 provides information on the precision of the ellipsometric angles for the (110) Si surface, where ($\psi_{pp}$, $\Delta_{pp}$) and ($\psi_{ps}$, $\Delta_{ps}$) are obtained using Eqs. (1) and (3), respectively. The single energy (3.45 eV) data in Fig. 4 were extracted from spectra collected in real time during exposure to humid air, after first etching the surface *in situ* to remove the oxide and then drying it with a $N_2$ flow. The RD signal shown in the bottom panel of Fig. 4 is computed from the four term average of $(\Delta\varepsilon)d$. The decrease in $\Delta_{pp}$ with time in Fig. 4 is attributed to the

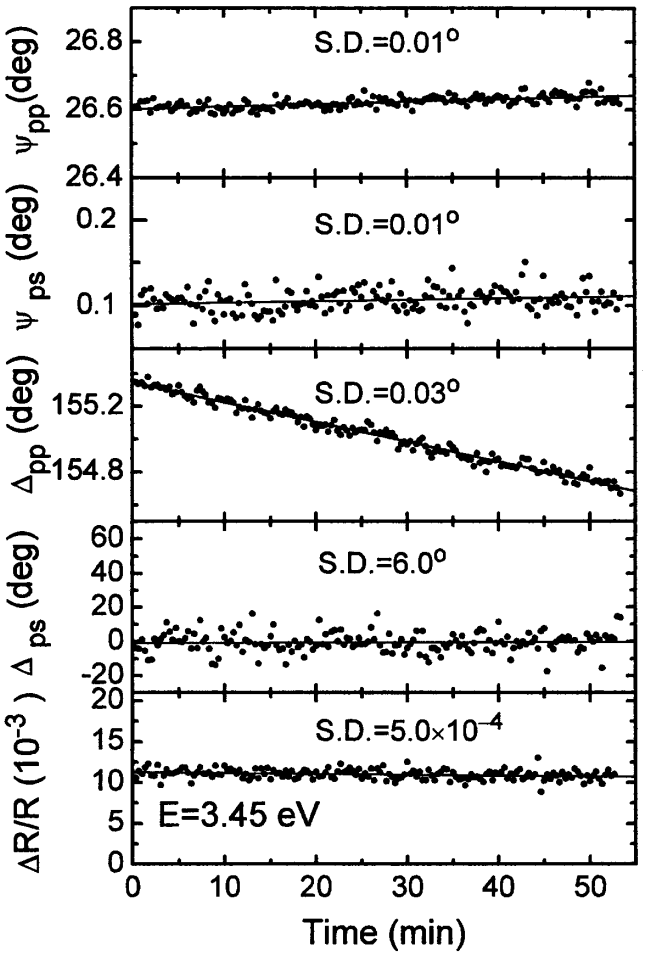


FIG. 4. Time evolution of ($\psi_{pp}$, $\Delta_{pp}$) and ($\psi_{ps}$, $\Delta_{ps}$) at 3.45 eV extracted from spectra in $\rho_{pp}$ and $\rho_{ps}$ both collected in 12 s during exposure of initially clean (110) Si to a flow of humid air. Also shown are the associated $\theta_a = 0°$ RD data computed from $\mathrm{Im}[(\Delta\varepsilon)d]$. The values indicate standard deviations from the linear fits.

adsorption of water molecules on the surface, which has no significant effect on the surface anisotropic response at 3.45 eV [3]. The values presented in Fig. 4 are the standard deviations from best fit linear trends. The temporal standard deviation in $\Delta R/R$ of $5 \times 10^{-4}$ approaches the performance obtained by scanning RDS from fixed samples [4].

The solid lines in the lower two panels of Fig. 3 represent results of a Kramers-Kronig consistent optical model for $\Delta\varepsilon$. This model starts with an analytical expression for the bulk isotropic dielectric function of silicon from 2.0 to 4.6 eV, based on three generalized oscillators [10]. In the fitting, the following characteristics of the uniaxial surface layer are assumed to differ, not only in the two principal crystal directions, $[1\bar{1}0]$ and [001], but also from those of the bulk: (i) the $E_1$ and $E_2$ critical point resonance energies (bulk values of 3.38 and 4.29 eV) and the energy of a broad intermediate resonance (bulk value of 3.63 eV), (ii) the associated three broadening parameters,

TABLE I. Characteristics of the three-oscillator fit of Fig. 3 for the $E_1$ and $E_2$ transitions, including the differences in resonance energies $E$ and broadening parameters $\Gamma$. The subscript "$b$" denotes the bulk values, whereas "$1\bar{1}0$" and "001" denote values appropriate for electric fields vibrating along the indicated principal crystal axes.

| Surface—bulk critical point differences | Critical points $E_1$ | $E_2$ |
|---|---|---|
| $E_{1\bar{1}0} - E_b$ (eV) | $-0.01 \pm 0.01$ | $-0.11 \pm 0.01$ |
| $E_{001} - E_b$ (eV) | $0.08 \pm 0.02$ | $0.02 \pm 0.05$ |
| $\Gamma_{1\bar{1}0} - \Gamma_b$ (eV) | $-0.01 \pm 0.01$ | $0.00 \pm 0.01$ |
| $\Gamma_{001} - \Gamma_b$ (eV) | $0.06 \pm 0.01$ | $0.11 \pm 0.03$ |

and (iii) $\varepsilon_{1\infty}$, the constant contribution to $\varepsilon_1$. The amplitudes, exponents, and phases of the generalized oscillators are assumed to remain unchanged from the bulk, and the magnitude of $(\Delta\varepsilon)d$ is determined from $\Delta\varepsilon_{1\infty}$ and $d$, which are both varied in the fitting. The excellent fit in Fig. 3 with $d = 4.2 \pm 0.75$ Å supports the four term averaging for $(\Delta\varepsilon)d$. The best fit parameters for the $E_1$ and $E_2$ critical points are given in Table I. The energy shifts demonstrate that the bulk critical points exhibit dichroic surface behavior, possibly due to surface-induced strain and/or modifications in electric field [11].

In summary, we have applied a dual rotating-compensator multichannel ellipsometer for high speed Mueller matrix spectroscopy of bulk and thin film semiconductors. In this study, as an illustrative example, the spectra in the Mueller matrix measured for (110) Si in reflection at an incidence angle near 70° have been applied to derive spectra, not only in the bulk isotropic dielectric function $\varepsilon_b$, but also in the surface anisotropic response $\Delta\varepsilon$ and the degree of polarization $p$ of the reflected beam. The results are clearly consistent with surface-induced optical anisotropy having uniaxial symmetry. The advantages of the new instrument include the ability to perform spectroscopic measurements in real time, and to deduce $\varepsilon_b$, $\Delta\varepsilon$, and $p$ simultaneously with a single instrument and a fixed sample. In fact, extensions to other surface anisotropies (e.g., those that are morphological in nature) and to bulk anisotropies in semiconductors are of immediate interest. Future efforts will involve enhancement of instrument precision for higher speed spectroscopy.

The authors acknowledge support of the National Science Foundation (Grant No. DMR-0137240) and the National Renewable Energy Laboratory (Subcontract No. AAD-9-18-668-09).

[1] F. Wooten, *Optical Properties of Solids* (Academic, New York, 1972).
[2] R.W. Collins, I. An, H. Fujiwara, J. Lee, Y. Lu, J. Koh, and P.I. Rovira, Thin Solid Films **313–314**, 18 (1998).
[3] D. E. Aspnes, J. Vac. Sci. Technol. B **3**, 1498 (1985).
[4] B. Drévillon and V. Yakovlev, Phys. Thin Films **19**, 1 (1994).
[5] M. Ebert, K. A. Bell, S. D. Yoo, K. Flock, and D. E. Aspnes, Thin Solid Films **364**, 22 (2000).
[6] R.W. Collins and J. Koh, J. Opt. Soc. Am. **16**, 1997 (1999).
[7] J. Lee, J. Koh, and R.W. Collins, Rev. Sci. Instrum. **72**, 1742 (2001).
[8] M. Schubert and W. Dollase, Opt. Lett. **27**, 2073 (2002).
[9] K. Hingerl, D. E. Aspnes, I. Kamiya, and L. T. Florez, Appl. Phys. Lett. **63**, 885 (1993).
[10] J. Leng, J. Opsal, H. Chu, M. Senko, and D. E. Aspnes, Thin Solid Films **313–314**, 132 (1998).
[11] U. Rossow, L. Mantese, and D. E. Aspnes, J. Vac. Sci. Technol. B **14**, 3070 (1996).